Solution biophysics identifies lipid nanoparticle non-sphericity, polydispersity, and dependence on internal ordering for efficacious mRNA delivery

Marshall S. Padilla[1], Sarah J. Shepherd[1], Andrew R. Hanna[1], Martin Kurnik[2], Xujun Zhang[2], Michelle Chen[2], James Byrnes[3], Hannah M. Yamagata[1], Adele Ricciardi[4], Ryann A. Joseph[1], Kaitlin Mrksich[1], David Issadore[1,5,6], Kushol Gupta[7*], Michael J. Mitchell[1,8,9,10,11,12,13*]

[1]Department of Bioengineering, University of Pennsylvania, Philadelphia, PA 19104, USA.
[2]Wyatt Technology, LLC, Goleta, CA 93117, USA.
[3]National Synchrotron Light Source II, Brookhaven National Laboratory, Upton, NY 11973, USA
[4]Department of Surgery, University of Pennsylvania Health System, Philadelphia, PA 19104, USA.
[5]Department of Chemical and Biomolecular Engineering, University of Pennsylvania, Philadelphia, PA 19104, USA.
[6]Department of Electrical and Systems Engineering, University of Pennsylvania, Philadelphia, PA 19104, USA.
[7]Department of Biochemistry and Biophysics, Perelman School of Medicine, University of Pennsylvania, Philadelphia, PA 19104, USA.
[8]Abramson Cancer Center, Perelman School of Medicine, University of Pennsylvania, Philadelphia, PA 19104, USA.
[9]Center for Cellular Immunotherapies, Perelman School of Medicine, University of Pennsylvania, Philadelphia, PA 19104 USA.
[10]Penn Institute for RNA Innovation, Perelman School of Medicine, University of Pennsylvania, Philadelphia, PA 19104, USA.
[11]Institute for Immunology, Perelman School of Medicine, University of Pennsylvania, Philadelphia, PA 19104, USA.
[12]Cardiovascular Institute, Perelman School of Medicine, University of Pennsylvania, Philadelphia, PA 19104, USA.
[13]Institute for Regenerative Medicine, Perelman School of Medicine, University of Pennsylvania, Philadelphia, PA 19104, USA.
*Co-Corresponding authors: kgupta@pennmedicine.upenn.edu; mjmitch@seas.upenn.edu

Keywords

Lipid nanoparticles, mRNA, small-angle X-ray scattering, field-flow fractionation, multiangle light scattering, analytical ultracentrifugation

Abstract

Lipid nanoparticles (LNPs) are the most advanced delivery system currently available for RNA therapeutics. Their development has accelerated since the success of Patisiran, the first siRNA-LNP therapeutic, and the mRNA vaccines that emerged during the COVID-19 pandemic. Designing LNPs with specific targeting, high potency, and minimal side effects is crucial for their successful clinical use. These characteristics have been improved through the development of microfluidic platforms, which have enhanced the efficacy and uniformity of LNP batches. However, our understanding of how the composition and mixing method influences the structural, biophysical, and biological properties of the resulting particles remains limited, hindering the development of LNPs. Our lack of structural understanding extends from the physical and compositional polydispersity of LNPs, which render traditional characterization methods, such as dynamic light scattering (DLS), unable to accurately quantitate the physicochemical characteristics of LNPs. In this study, we address the challenge of structurally characterizing polydisperse LNP formulations using emerging solution-based biophysical methods that have higher resolution and provide biophysical data beyond size and polydispersity. These techniques include sedimentation velocity analytical ultracentrifugation (SV-AUC), field flow fractionation followed by multi-angle light scattering (FFF-MALS), and size-exclusion chromatography in-line with synchrotron small-angle X-ray scattering (SEC-SAXS). Here, we show that the LNPs have intrinsic polydispersity in size, RNA loading, and shape, and that these parameters are dependent on both the formulation technique and lipid composition. Lastly, we demonstrate that these biophysical methods can be employed to predict transfection in three biological

models by examining the relationship between mRNA translation and physicochemical characteristics. We envision that employing solution-based biophysical methods will be essential for determining LNP structure-function relationships, facilitating the creation of new design rules for future LNPs.

Introduction

Lipid nanoparticles (LNPs) have emerged as the preeminent non-viral drug delivery vehicle for nucleic acids, such as messenger RNA (mRNA), and are utilized for vaccines, protein replacement therapies, and gene therapy[1–3]. Their success has been demonstrated by the U.S. FDA approval of an siRNA LNP therapeutic, Alnylam Pharmaceutical's Onpattro™, and the FDA approval of two COVID-19 mRNA LNP vaccines, Moderna's Spikevax™ and Pfizer/BioNTech's Comirnaty™[4]. LNPs typically consist of four lipid components: an ionizable lipid, a phospholipid, a cholesterol, and a lipid-anchored PEG, which all contribute to LNP structure, size, and RNA encapsulation[5]. The formulation of LNPs occurs via rapid mixing of an ethanol phase containing the lipids and a low pH aqueous phase containing RNA. At a small scale, this is accomplished by microfluidic mixing devices or pipette mixing[6,7]. Changes in lipid composition and production methods can significantly impact LNP structure and physiochemical properties, which ultimately determine LNP stability, performance, and biodistribution *in vivo*[8]. For example, size varies between 50–200 nm based on formulation method and lipid structures[9,10]. Previous studies have demonstrated that microfluidic mixing devices, such as those incorporating staggered herringbone micromixer architectures, can improve control over desirable LNP physical properties, such as size, size distribution, and RNA encapsulation efficiency[11,12]. Furthermore, the laminar flow conditions employed in these microfluidic devices enables a rapid, controlled, and reproducible fluidic profile where microfluidic-generated LNPs can be significantly more potent than bulk mixed LNPs for mRNA delivery[13].

Although novel formulation modalities can enhance the efficacy of LNPs, understanding the mechanism underlying these improvements is hindered by the current characterization practices, which suffer from low sensitivity and resolution[14]. For example, traditional characterization techniques cannot differentiate between empty LNPs containing no RNA and RNA-containing LNPs; thus, it is difficult to accurately describe RNA loading efficiencies and heterogeneity within a sample[15]. Batch mode dynamic light scattering (DLS), a common technique to characterize LNP size distributions, cannot differentiate these subpopulations, cannot discern asphericity, has limited resolution for these typically polydisperse samples, and is biased towards larger species. Similarly, cryo-TEM is unable to differentiate loaded and unloaded LNPs and may not accurately describe LNP morphology and structure since LNPs are evaluated in a vitrified state prepared onto a grid that may not be representative of LNPs in solution. Recent studies using fluorescently-tagged RNA and lipids have found that up to 80% of LNPs in a given mRNA LNP sample are empty[16–18]. Traditional characterization methods using absorbance or fluorescence assays, including the RiboGreen™ RNA quantitation assay, can detect RNA but cannot determine RNA loading on an individual particle basis[19,20]. None of these methods can resolve the nature of the hexagonal phase (H_{II}) of the RNA-lipid interface within the LNP, which has been shown to be critical for achieving effective transfection[21].

Hence, current efforts to define concrete relationships between the biological efficacy of a formulation with the individual lipid structures, excipient ratios, formulation technique, and physiochemical characteristics have yielded weak and conflicting correlations. This has created the need for examining hundreds or thousands of different formulations in a trial-by-error fashion to find an LNP that meets the intended application parameters. While several studies have emerged in the past five years employing more advanced characterization strategies, they are focused on a single technique that cannot fully describe the complex nature of LNPs. Moreover, many current strategies require fluorescent tags that can unintentionally alter the LNP itself. Lastly, several methods often rely on assuming LNPs adopt a spherical morphology, whereas recent work has suggested that LNPs likely adopt a more elongated structure[22]. Thus, there is a pressing need to modernize the current LNP analytical repertoire by employing multiple techniques that can discriminate sub-populations within LNP samples.

Here, we employ an array of label-free solution-based biophysical techniques including sedimentation velocity analytical ultracentrifugation (SV-AUC), field-flow fractionation combined with multiangle light scattering (FFF-MALS), and size exclusion chromatography in-line with synchrotron small-angle X-ray scattering (SEC-SAXS) (Figure 1). We apply these techniques in concert to characterize a small library of gold standard LNPs that differ

in their lipid excipients and formulation techniques to provide a more holistic representation of LNP size distribution, loading, shape, and ordering. Lastly, we demonstrate the utility of these strategies in predicting LNP transfection in primary human T cells, intravenous delivery, and intramuscular delivery. This work not only implements orthogonal techniques to uncover LNP characteristics and structure-activity relationships, but also establishes a workflow to probe LNPs with increasing resolution, starting from whole formulation analysis of particle size and loading to inner particle assembly.

Results

Formulation and traditional characterization of the LNP library

Four representative LNP formulations were chosen based on their clinical significance and status as "gold standards". Names were assigned according to the incorporated ionizable lipid, include MC3 (Alnylam), C12-200 (academic), SM-102 (Moderna), ALC-0315 (Pfizer/BioNTech), and were prepared with firefly (FLuc) luciferase mRNA. Moreover, each LNP was formulated utilizing pipette mixing (*i.e.*, bulk mixing) or our established 1X polydimethylsiloxane microfluidic devices[13]. Microfluidic LNPs containing no mRNA were also created as controls, for a total of twelve LNPs. The particles were characterized using standard techniques to evaluate mRNA concentration and encapsulation efficiency, size, size distribution, ζ-potential, relative pK_a, and morphology. Encapsulated mRNA concentration and relative encapsulation efficiencies were determined by the fluorescent RiboGreen RNA quantitation assay, where the microfluidic-formulated LNPs had mRNA concentrations of 40–60 ng/μL and encapsulation efficiencies >80%, while bulk mixed LNPs had lower mRNA concentrations of 10–30 ng/μL and encapsulation efficiencies of ~50% (Figure 2A–B). One exception to these trends were the C12-200 LNPs, which maintained the same mRNA concentration of ~45 ng/μL for both formulation methods, while the relative encapsulation efficiencies for MC3, SM-102, and ALC-0315 were markedly lower at 40–60%. DLS in combination with static light scattering revealed that the microfluidic-formulated LNPs had ~40 nm hydrodynamic radii with LNP concentration ~10^{12} LNP/mL, whereas the bulk mixed LNPs had larger hydrodynamic radii of ~100 nm as well as a smaller LNP concentration of ~10^{11} particles/mL (Figure 2C–D). ζ-potential measurements indicated that all LNPs had an approximately neutral charge (Figure 2E). Apparent pK_a was determined by a fluorescent 6-(*p*-toluidino)-2-naphthalenesulfonic acid (TNS) assay, where pK_a values were ~6 (Figure 2G). Cryogenic transmission electron microscopy (cryo-TEM) imaging was performed to evaluate LNP morphology (Figure 2G). Generally, microfluidic-formulated LNPs maintained a uniform electron dense core with narrower size distributions than bulk mixed LNPs, which had more variable size and internal structure, with some aqueous compartments. Of note, the C12-200 LNP formulations

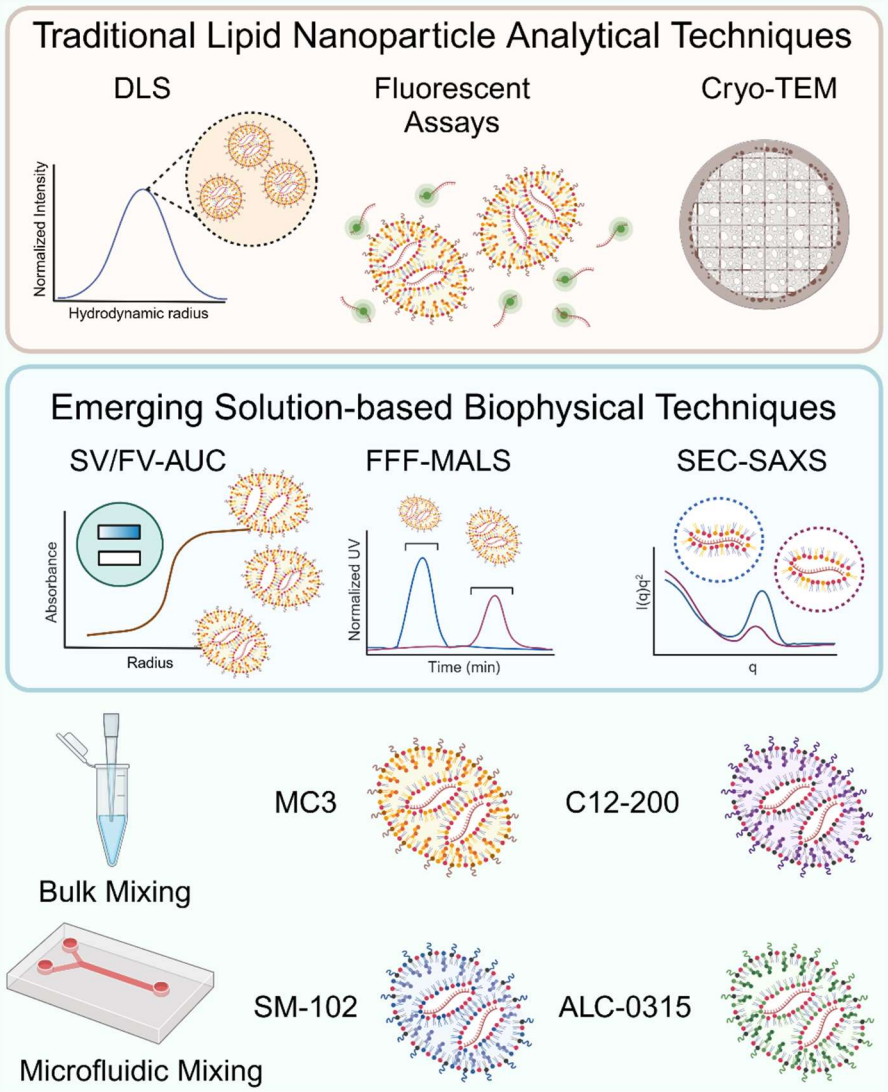

Figure 1. Experimental summary. Comparison of techniques to analyze physiochemical characteristics and morphology and lipid nanoparticles (LNPs; top). LNP library consisting of two different mixing methods and four different gold standard formulations (bottom). Created in BioRender. Hamilton, A. (2024) https://BioRender.com/b36w964.

had distinct multilamellar ring structures that were not observable for other lipid formulations that contained an amorphous core with an exterior bilayer.

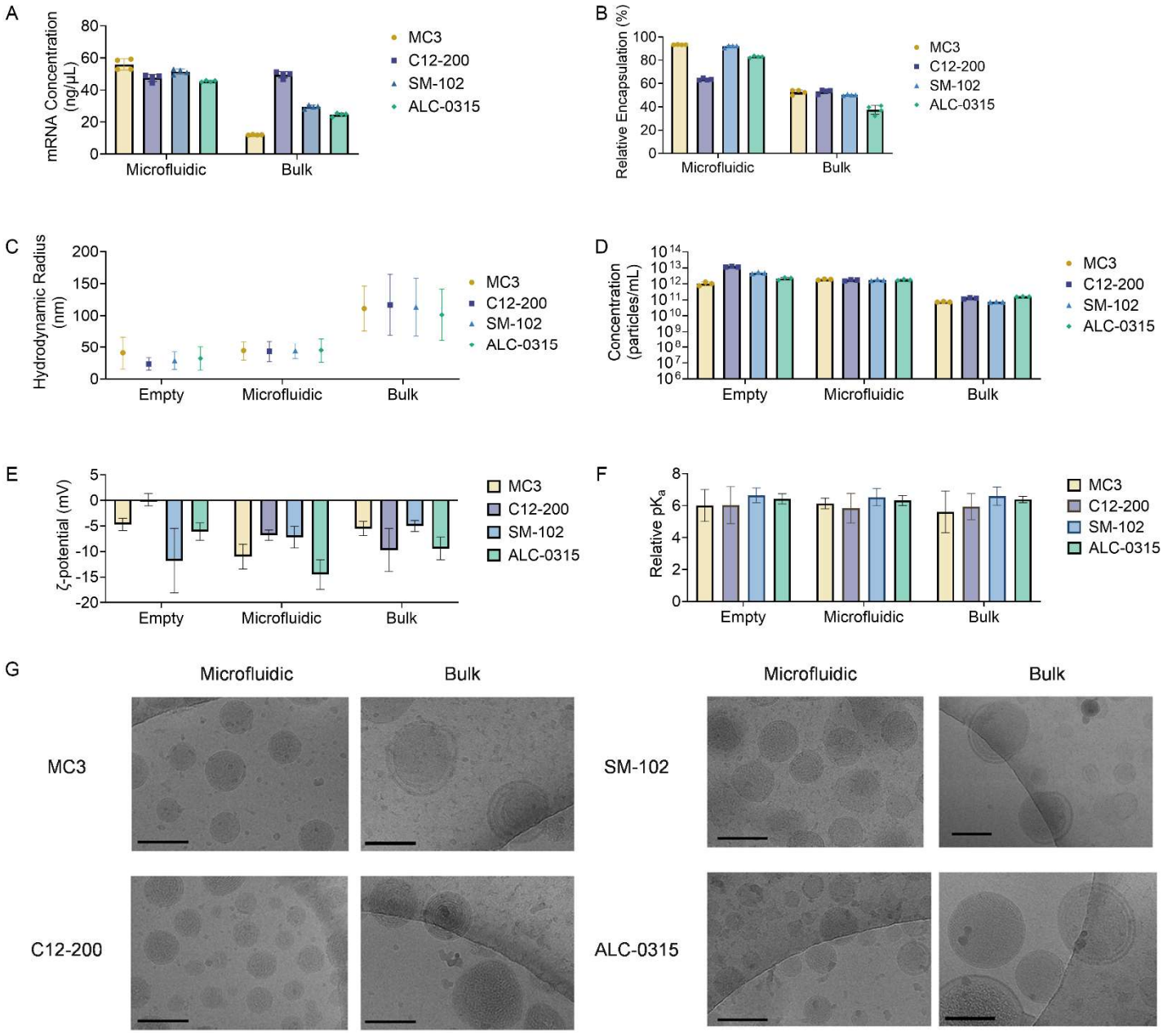

Figure 2. Traditional physicochemical characterization of lipid nanoparticles (LNPs). A–G, LNP physicochemical characterization of **(A)** mRNA concentration and **(B)** relative encapsulation efficiency determined by a RiboGreen assay, **(C)** hydrodynamic radius and **(D)** particle concentration obtained via DLS, **(E)** ζ-potential calculated via electrophoretic light scattering, **(F)** apparent pK_a determined by a 6-(*p*-toluidino)-2-naphthalenesulfonic acid (TNS) assay, and **(G)** morphology utilizing cryogenic transmission electron microscopy. Measurements are reported as mean ± SD of n = 4 technical replicates for A–B and n = 3 technical replicates for C–F. Scale bar corresponds to 100 nm. Source data are provided as a Source Data file.

Analysis of LNP encapsulation polydispersity using analytical ultracentrifugation

While DLS can be used to assess particle size and detect polydispersity, DLS lacks the capability to resolve individual populations in polydisperse samples[23]. In contrast, analytical ultracentrifugation is a quantitative, first principle approach that is sensitive to particle size, shape, and density[24]. It has been demonstrated that proper AUC implementation does not induce enough shear force to lyse the LNP and instead, can provide insights into LNP polydispersity not apparent by DLS analysis[25]. Moreover, with density matching methods, compositional

informational and RNA loading can be derived[15,26]. The sedimentation properties of this LNP panel were assessed using sedimentation/flotation velocity analytical ultracentrifugation (SV/FV-AUC). Because this approach is sensitive to the density of the solutes examined, the tool can readily discriminate unloaded LNPs that float versus those loaded with the denser mRNA payload that increase sedimentation. AUC is non-destructive and does not require chemical alterations like a fluorescent label, relying instead on the intrinsic absorption properties of the LNPs for detection.

The results from this analysis are shown in Figure 3. Each sample in the panel was characterized by DLS and subsequently also analyzed by AUC. Modest rotor speeds were applied with the UV detection optimized for detection of ribonucleic acid bases (260 nm) at 20 °C. In the primary data, evidence for both flotation and sedimentation are readily observed (Supplementary Figure 1). A least-squares *g*(s)* model[27] was applied to assess the presence of both floating and sedimenting species[28]. The multimodal appearance of the distributions suggests the existence of subpopulations of particles that were not detected by DLS. In line with other studies, most of the detected mass for the MC3, SM-102, and ALC-0315 LNPs were found to float, with S values spanning 0 to -200S. In contrast, the C12-200 LNPs predominantly sediment, with S values spanning 0 to ~100S. These trends are well in-line with the published densities of these four ionizable lipids (0.95, 0.94, 0.89, and 1.03 g/cm^3, respectively). In each case, the microfluidic samples display far less polydispersity than the bulk mixed samples.

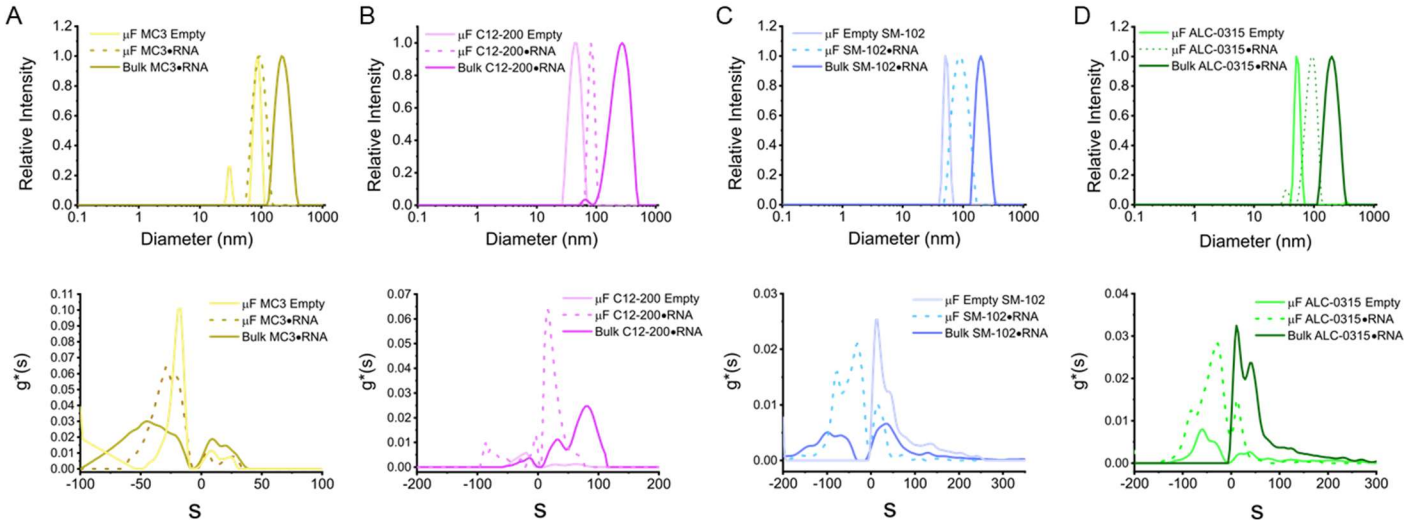

Figure 3. Analysis of LNPs by dynamic light scattering (DLS) and analytical ultracentrifugation (AUC). A–D, In the upper panels, DLS distributions are shown for microfluidic empty LNPs (dotted line), microfluidic mRNA LNPs (dark line), and bulk mixed mRNA LNPs for each of four ionizable lipids: **(A)** MC3, **(B)** C12-200, **(C)** SM-102, and **(D)** ALC-0315. Diameter in nanometers is shown on the x-axis and relative intensity on the y-axis. In the lower panels, ls-g*(s) distribution profiles from analytical ultracentrifugation (AUC) analysis are shown for the same samples, using the program SEDFIT[29]. Species observed to the left of zero represent floating species while those to the right represent sedimenting species, with the area under the curve proportional to the relative abundance in the formulation. Source data are provided as a Source Data file.

Multiangle Light Scattering Analysis

Both DLS and AUC are sensitive to the shape of macromolecules in solution. While the Stokes-Einstein[30] and Svedberg[31] equations can be applied to extrapolate size and indirectly, mass, accounting for anisotropy in shape, size, and density within polydisperse mixtures and differences in composition, including with mRNA and lipids, makes the determination of these parameters more challenging. Recent studies suggest that LNPs tend to assume a more ellipsoidal character, likely due to their bleb-like architecture, which complicates the interpretation of data from these methods[22,32]. To more accurately determine molecular weight and measure polydispersity without this confounding issue, we applied field-flow fractionation in-line with multi-angle light scattering (FFF-MALS) to our LNP panel.

Multi-angle light scattering (MALS), coupled with UV and refractive index (RI) detection, provides size, molar mass (or molecular weight, MW), polydispersity, concentration, and compositional information for composite particles like LNPs, independent of the effects of shape[33]. However, a key factor in its application is the separation

method used prior to data collection, which is typically achieved via chromatography for smaller macromolecules[34]. By applying field-flow fractionation (FFF), superior separation of larger particles in the 1–1000 nm range, such as LNPs, is achieved under gentler conditions compared to chromatographic methods[35]. Additionally, particle-column interactions that could alter observable properties are minimized due to the absence of a stationary phase. The ideal size-based FFF separation enables proper measurement of polydispersity of MW, size, and payload by the online detectors[33].

The results of this analysis are provided in Table 1 and Figure 4. The fractograms for each separation reflect the relative abundance of analytes fractionated by this method. In each case, a major peak representing the bulk of the LNP mass is observed during the separation. However, these profiles are relatively broad and, in some cases, asymmetric, indicating the presence of additional subpopulations in the formulation. Consistently, the retention times for bulk-mixed particles were broader and longer than those for particles prepared using microfluidics. As expected for polydisperse samples, the molar mass measured by FFF-MALS increases with retention time, spanning approximately 1–2 orders of magnitude in the megadalton range for all formulations examined. Bulk-mixed samples consistently displayed 10 to 20-fold higher masses. Mass concentrations for the mRNA and lipid components were determined using a previously described strategy for correcting the concentration measurements for UV scattering from the LNPs[33]. Microfluidic particles consistently contained 4–30 times higher mRNA concentration than bulk-mixed particles. While the mRNA component is present throughout the microfluidic peak, in bulk samples it appears to partition into smaller particle populations, disappearing rapidly with larger sizes. The bulk-mixed SM-102 sample contains the largest particles of all the samples, with higher molar masses (~10^9–10^{10} Da) than the particles in the other samples. Hence, a substantially higher nucleic acid number is observed for these particles.

Interestingly, empty particles prepared by microfluidic methods were larger in mass and hydrodynamic radius (R_h) compared to loaded microfluidic LNPs, with greater polydispersity as evidenced by M_w/M_n (dispersity, Đ), where values between 1.5–2.0 correspond to moderately polydisperse samples and values >2.0 indicate broad polydispersity. This suggests that the mRNA payload may influence the organization of the particle more than the lipid exterior. Consistently, microfluidic LNPs displayed hydrodynamic radii (R_h) that were 1.5 to 2-fold smaller than bulk mixed LNPs, and geometric radii ($R_{geometric}$) that were 2–3-fold smaller. $R_{geometric}$ assumes a spherical shape and differs from the radius of gyration (R_g), while R_h describes the effective radius of the particle based on its diffusion properties. Overall, FFF-MALS can resolve the true dispersity of these multimodal, polydisperse samples, quantified as the ratio between the weight-average and number-average molar mass (M_w/M_n). M_w/M_n from MALS correlates more closely with the observed variations in mass and composition than the PDI values derived from DLS, which are based on intensity-weighted mean hydrodynamic diameters obtained by fitting the autocorrelation function data to a model that incorrectly assumes that the sample contains a single particle population and in contrast, indicate misleadingly low polydispersity.

Table 1. Physicochemical parameters of the lipid nanoparticles (LNPs) obtained by field-flow fractionation multi-angle light scattering (FFF-MALS)

LNP	R_h (nm)	$R_{geometric}$ (nm)	M_w (MDa)	M_w/M_n	mRNA (ng/µL)	Nucleic Acid Number	Lipid (mg/mL)
$MC3^{\mu F \bullet empty}$	55.7 ± 18.9	76.5 ± 18.6	222.8 ± 201.7	2.01 ± 1.33	-	-	-
$MC3^{\mu F \bullet FLuc}$	46.7 ± 0.5	50.7 ± 0.3	153.3 ± 3.1	1.48 ± 0.04	68 ± 5	32.8 ± 2.9	0.608 ± 0.03
$MC3^{Bulk \bullet FLuc}$	78.5 ± 0.1	105.1 ± 0.3	1368 ± 21	1.81 ± 0.05	17 ± 3	31.0 ± 6.3	0.668 ± 0.012
$C12\text{-}200^{\mu F \bullet empty}$	70.8 ± 9.5	87.8 ± 10.6	245.2 ± 120.8	3.67 ± 2.2	-	-	-
$C12\text{-}200^{\mu F \bullet FLuc}$	59.2 ± 2.5	56.4 ± 3.4	123.8 ± 4.5	1.73 ± 0.08	39 ± 4	14.6 ± 5.1	0.583 ± 0.028
$C12\text{-}200^{Bulk \bullet FLuc}$	84.5 ± 0.5	123.9 ± 0.8	2459 ± 77	1.65 ± 0.06	4 ± 1	20.5 ± 4.9	0.210 ± 0.003
$SM\text{-}102^{\mu F \bullet empty}$	74.9 ± 10.3	99.8 ± 10.1	503.7 ± 319.2	3.28 ±1.28	-	-	-

SM-102$^{\mu F \bullet FLuc}$	49.9 ± 5.4	60.7 ± 8.7	170.1 ± 32.0	1.47 ± 0.24	41 ± 6	33.5 ± 9.5	0.350 ± 0.037
SM-102$^{Bulk \bullet FLuc}$	102.0 ± 3.0	147.8 ± 2.0	4618 ± 410	1.07 ± 0.03	30 ± 1	200.5 ± 26.7	0.069 ± 0.014
ALC-0315$^{\mu F \bullet empty}$	72.1 ± 29.0	72.7 ± 25.0	75.9 ± 29.7	2.62 ± 1.06	-	-	-
ALC-0315$^{\mu F \bullet FLuc}$	40.6 ± 0.4	41.6 ± 0.1	84.8 ± 1.3	1.77 ± 0.01	86 ± 1	14.2 ± 0.5	0.869 ± 0.017
ALC-0315$^{Bulk \bullet FLuc}$	76.5 ± 0.5	104.0 ± 0.4	1106 ± 19	3.21 ± 0.14	2.6 ± 0.4	2.2 ± 0.6	0.275 ± 0.025

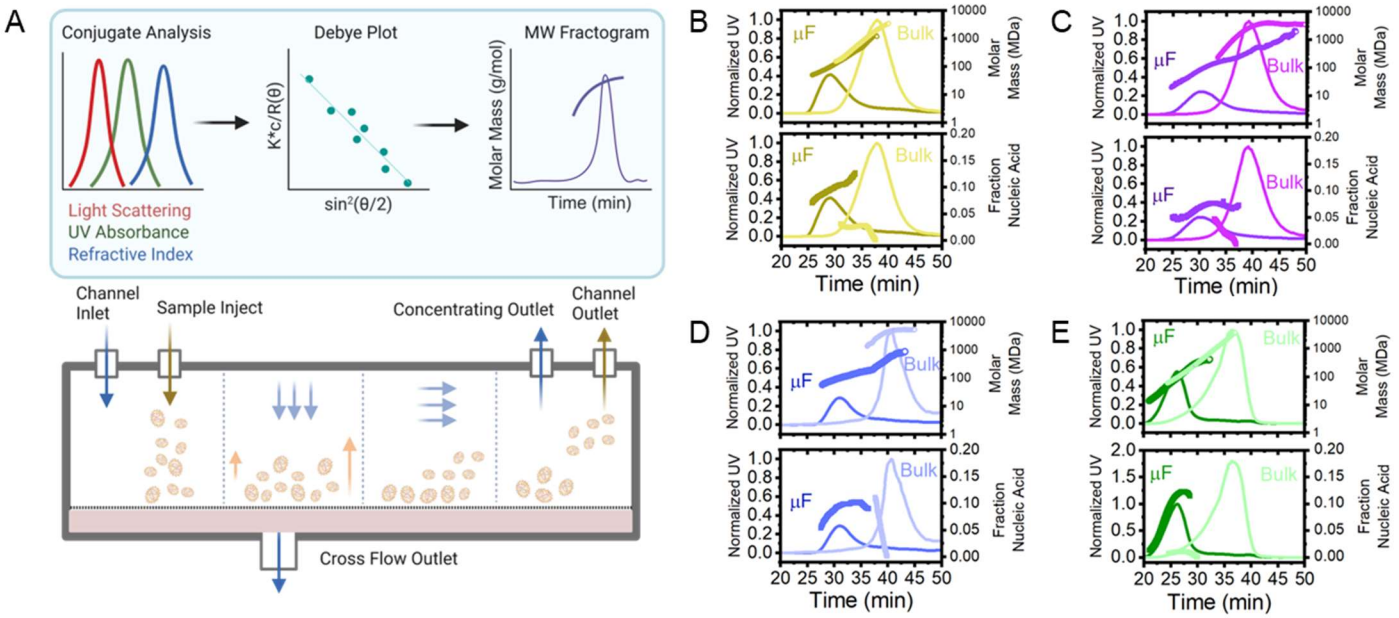

Figure 4. Size distribution and compositional heterogeneity of LNPs as determined by field-flow fractionation multi-angle light scattering (FFF-MALS). A, diagram of FFF and LNP analysis processes (left). **B–E,** in each panel, both the determined molar mass profiles (upper panels, spheres) and mRNA weight fraction (lower panels, spheres) derived from MALS analysis for microfluidic (dark solid line) and bulk mixed (light solid line) particles were overlaid with UV fractograms from in-line FFF separations. Quadrants represent **(B)** MC3, **(C)** C12-200, **(D)** SM-102, and **(E)** ALC-0315. Additional parameters derived from these analyses are provided in Table 1. **A,** Created in BioRender. Hamilton, A. (2024) https://BioRender.com/f01w633. Source data are provided as a Source Data file.

Small-angle X-ray Scattering Analysis

Small-angle X-ray scattering (SAXS) is a free-solution measurement particularly well-suited for probing the internal structure of LNPs. This is due in part because the scattering length density of the electron-dense nucleic acid component is significantly higher than that of the lipid when exposed to X-rays. In addition to the size and shape information captured at lower scattering angles, higher scattering angle features, such as Bragg peaks, can provide detailed insights into lipid packing and spacing within the particle[36]. Previous studies have shown that LNPs exhibit a characteristic first-order Bragg peak at a scattering vector (q) of approximately 0.1–0.15 Å^{-1}, corresponding to a distance (d) of ~41.9–62.8 Å, where $d = \frac{2\pi}{q}$, indicative of a highly ordered internal structure. These length scales are generally consistent with what would be predicted for well-ordered stacked lipid bilayers comprised of any of the four ionizable lipids examined here (~40–50 Å). Prior work has established models for LNP structures composed of bilayers with a disordered core or multilamellar particles, which can be discerned by the spacing of these Bragg peaks[37–39]. The structure of the core has been directly linked to *in vivo* delivery and uptake[8].

To date, most reported SAXS measurements of LNP particles have been conducted under equilibrium conditions on bulk mixtures with very high particle concentrations, without accounting for the physical and chemical polydispersity of the formulations or validated by complementary free-solution methods other than DLS. Since the resulting scattering profiles represent the volume-weighted average of all scatterers within the X-ray path, we implemented two strategies in tandem to directly address this issue and enhance the information content of the experiment: (i) in-line size-exclusion chromatography (SEC) and (ii) singular value decomposition (SVD) analysis of the data (Figure 5A).

For each of the LNP preparations in our panel, we performed synchrotron SAXS measurements in-line with SEC, both with and without SVD analysis as incorporated in the program REGALS[40] and compared the results. In control experiments, we performed static measurements on microfluidic LNPs and did not observe concentration-dependent behavior or evidence of interparticle interference at particle concentrations of ~10^{11} or lower in serial dilutions (Supplementary Figure 2). Using UV-Vis data from an in-line diode detector array and the mean intensity of recorded X-ray scattering, raw data from this experiment showed strong UV absorbance at 260 nm, coinciding with X-ray scattering intensity between q ~0.1–0.15 $Å^{-1}$, which was separated from other scattering species via column separation (Supplementary Figure 3). As a control, microfluidic lipid-only particles were prepared and displayed no such peak feature. For each sample, approximately 70–100 scattering profiles collected from the elution peak were combined for subsequent analysis, either by averaging the selected profiles of the isocratically eluted peak or by analyzing the profiles using SVD to decompose the data into minimal components with maximal redundancy (Figure 5B–I, Supplementary Tables 1–4). For each LNP formulation, two to three significant components were readily identified through SVD analysis, and the data were decomposed accordingly. To further substantiate the statistical uniqueness of these SAXS data, we compared them using the Volatility of Ratio (V_r) metric, which describes the variability in the ratio of scattering intensity between two profiles and is advantageous over other methods of profile comparison, especially in regimes of weaker signals[41]. When applied to the data from these analyses and viewed as a heat map, different degrees of low similarity are observed between experimental profiles with or without SVD analysis and by method of preparation (Figure 6A). Together with the SVD analyses, this comparison indicates that the method employed here results in statistically significant differences in the resulting experimental profiles.

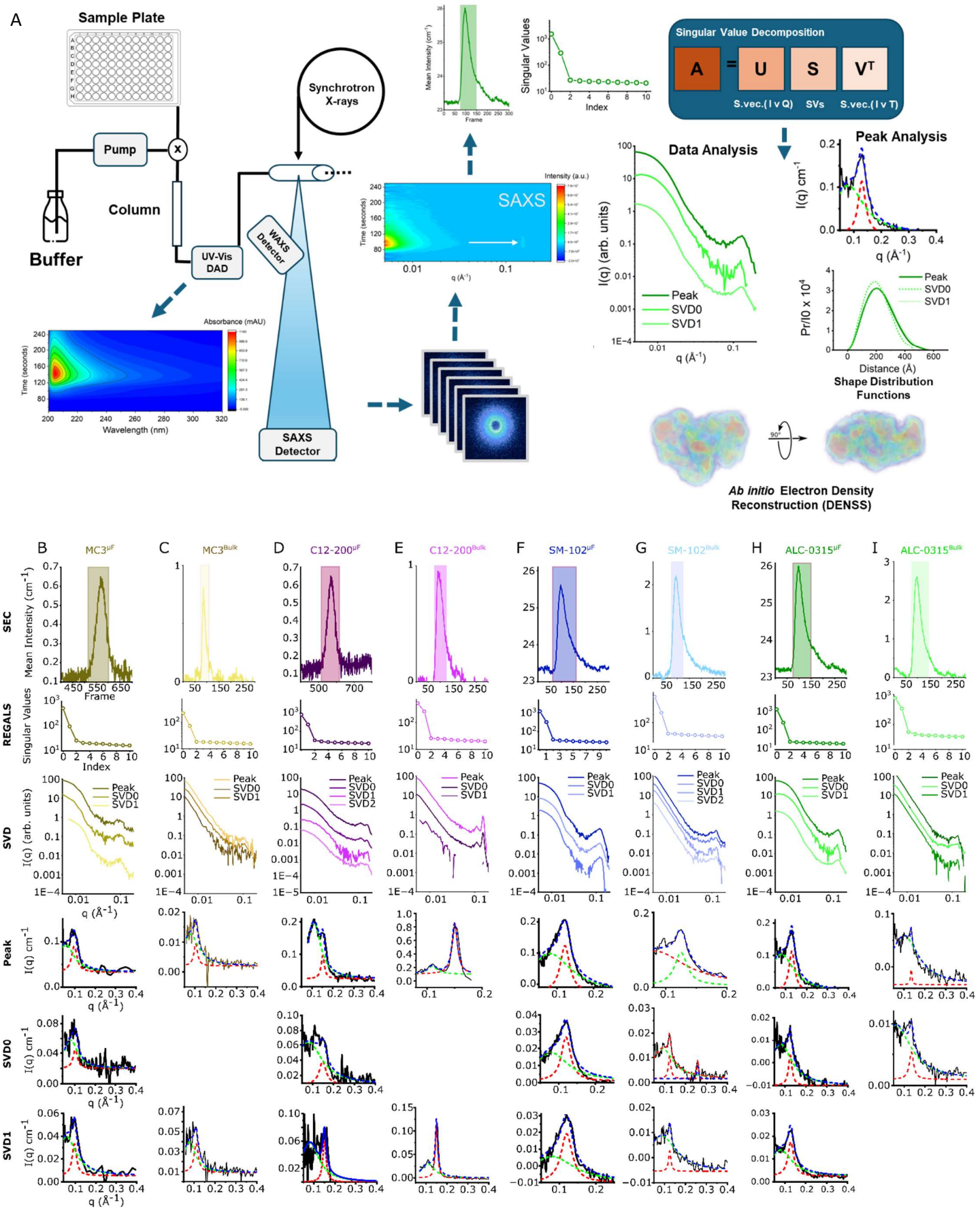

Figure 5. LNP batches contain discrete subspecies as identified by SEC-SAXS. A, Overview SEC-SAXS workflow to identify LNP subspecies. **B–I**, individual SEC-SAXS parameters for **(B)** MC3$^{\mu F}$, **(C)** MC3^{Bulk}, **(D)** C12-200$^{\mu F}$, **(E)** C12-200^{Bulk}, **(F)** SM-102$^{\mu F}$, **(G)** SM-102^{Bulk}, **(H)** ALC-0315$^{\mu F}$, **(I)** ALC-0315^{Bulk} LNPs. Each LNP underwent an identical processing protocol, involving identifying the main LNP peak in the SEC chromatogram (first row), selecting the number

of singular values (second row), scattering intensity of the main peak and corresponding singular values (third row), and fitting of the higher-q peak features (0.1 – 0.15 $Å^{-1}$) using multiple Lorentz peak feature (fourth, fifth, and sixth rows), where red is the first order Braggs peak fit, green is the disorder peak feature, and blue is the cumulative fit of the two features. Some SVD0 and SVD1 scattering plots were omitted due to low scattering signals. Source data are provided as a Source Data file.

These data were assessed in two complementary ways. First, the higher-q peak features between ~0.1–0.15 $Å^{-1}$ were analyzed using multiple Lorentz peak fitting[8] to deconvolve the signal of structural ordering from the overlapping disordered signal at larger length scales, providing measurements of peak width (FWHM) and magnitude (intensity at peak (I_p), area). Additionally, the size and shape of the particles were evaluated using the P(r) pair distance distribution function. Although Guinier analysis was not possible, the accessible q-range recorded in these experiments (q_{min} = 0.005 $Å^{-1}$) allowed for the assessment of the radius of gyration (R_g) and the maximum particle dimension (D_{max}) up to ~628 Å using P(r) analysis, in conditions where $q_{min} \leq \frac{2\pi}{D_{max}}$ (Figure 6B–E). These inverse Fourier transform analyses in turn facilitated the generation of three-dimensional *ab initio* shape reconstructions[22,42], providing a corroborating assessment of particle shape at low resolution.

We found that the shape of the scattering profile and location of the peaks was primarily determined by the lipid type and not by the mRNA payload or formulation method. For each lipid type, the first order Braggs peak is q_{peak} = 0.10 $Å^{-1}$, 0.16 $Å^{-1}$, 0.13 $Å^{-1}$, and 0.13 $Å^{-1}$, for lipid types MC3, C12-200, SM-102, and ALC-0315, respectively. Of the four ionizable lipids examined in this study, C12-200 is the most dissimilar from the others due to its five nitrogen atoms per molecule with a central ring, in contrast to only one nitrogen atom per molecule with longer chain alkyl tails for the other ionizable lipids. As such, two peaks appear in this q regime, where a smaller peak can be observed at q = 0.12 $Å^{-1}$ and a larger peak is present at q = 0.16 $Å^{-1}$. Due to the nature of size-exclusion separations, eluted particle concentrations were well below the initial injected particle concentrations of ~10^{11} particles/mL, precluding any interparticle interference while simultaneously facilitating a more detailed analysis of the lipid organization via the integral spacing of subsequent Braggs peak at higher q values, which requires high sample concentrations. The multiple Lorentz peak fitting allowed for resolution of the primary peak feature from overlapping signal at lower q values. Via this approach, we observed that microfluidic LNPs have higher intensity Bragg peak for three of the four ionizable lipids examined, upwards of ~2-fold for the averaged scattering from the SEC peak and upwards of ~10-fold higher for the SVD0 deconvoluted profiles; this higher intensity was concomitant with large peak area and width (Supplementary Table 3). We also noted that the formulation method has a measured impact on the peak position observed after the SEC enrichment step, indicating that some of the polydispersity inherent to these formulations map to the method by which the lipid-RNA structure assembles and the resulting internal structure.

Shape distribution analysis was only possible for microfluidic LNPs. To assist in a qualitative assessment of these distributions, we also collected equilibrium SAXS measurements on 60 nm silver and gold nanoparticles (Figure 6F–H, Supplementary Figure 4). Relative to these isotropic particles, the shape distribution functions generally displayed a greater skew of interatomic vectors to larger values relative to the peak (~R_g), suggestive of relatively anisotropic shapes, with the greatest anisotropy observed for the C12-200 particle. It has been recently demonstrated that the algorithm DENSS can be applied to SAXS data from LNPs to reconstruct *ab initio* low resolution electron density in three dimensions[22]. Applying this method to the SAXS data from the microfluidic particles, we can observe a core-shell structure with the electron rich mRNA within the core of the particles, surrounded by lower contrast lipids (Figure 6I–L). In the report by Dao and co-workers, “blebs” could be resolved[22]. In our study, no such regions were apparent from both data averaged across the SEC peak and after SVD analysis, suggesting that such species, which are observed on cryo-TEM grids, are resolved away by SEC. Consistent with the trends observed by P(r) analysis, anisotropic ellipsoids are observed for MC3, SM-102, and ALC-0315, whereas the C12-200 particles showed more prolate character. Overall, these data provide evidence for anisotropic particle shape in these formulations. Further corroborating these calculated shapes and their surface appearance are the determined Porod exponents from the primary data, which can be related to the surface and mass fractals of a particle[43,44]. The Porod region of the primary scattering profiles is defined by the region before the peak structural features (q < 0.1 $Å^{-1}$) and after the Guinier region (q > 0.01 $Å^{-1}$); the scattering in this region decays as $I(q) \propto q^{-P}$, where P is the Porod exponent that is dependent on particle shape[45]. For the MC3 and C12-200 particles, Porod exponents between 2–3 are observed, consistent with surface fractals reflecting possible disorder and porosity. The SM-102 and ALC-0315 particles have larger values between ~3–

4, consistent with a rough surface, but not consistent with a compact and smooth surface observed for the gold and silver nanoparticles (Px~4).

It has been recently demonstrated that the algorithm DENSS can be applied to SAXS data from LNPs to reconstruct *ab initio* low resolution electron density in three dimensions[22]. Applying this method to the SAXS data from the microfluidic particles, we can observe density consistent with a core-shell structure, with the electron rich mRNA within the core of the particles, surrounded by lower contrast lipids (Figure 6I–L). In the report by Dao and co-workers, “blebs” could be resolved[22]. In our study, no such regions were apparent from both data averaged across the SEC peak and after SVD analysis, suggesting that such species, which are observed on cryo-TEM grids, might be resolved away by SEC, or only occur in a very small percentage of particles and do not contribute strongly enough to the resultant scattering. Consistent with the trends observed by P(r) analysis, anisotropic ellipsoids are observed for MC3, SM-102, and ALC-0315, whereas the C12-200 particles showed more prolate character. Overall, these data provide evidence for anisotropic particle shape in these formulations.

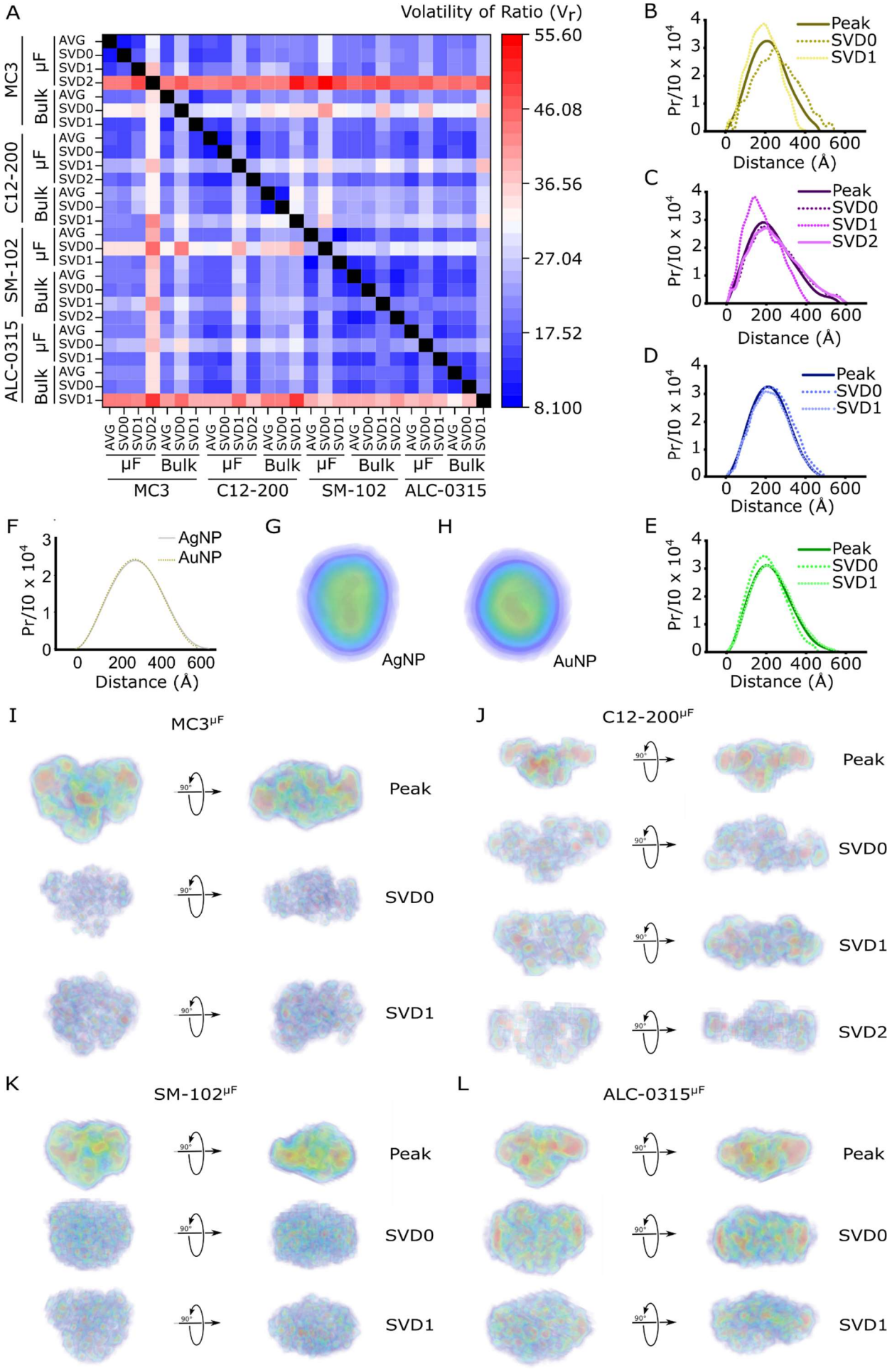

Figure 6. SEC-SAXS profiles have low degree similarity and reveal that LNPs adopt non-spherical morphologies. **A,** Volatility of Ratio (V_r) between the SEC-SAXS average peak and individual SVDs. **B–E,** P(r) analysis of the peak and SVDs for **(B)** MC3, **(C)** C12-200, **(D)** SM-102, and **(E)** ALC-0315 microfluidically mixed LNPs. **F,** P(r) analysis for 60 nm silver and gold spherical nanoparticles. **G–L,** DENsity from Solution Scattering (DENSS) *ab initio* electron density reconstructions from the SEC-SAXS profiles for **(G)** 60 nm silver spherical nanoparticles, **(H)** 60 nm gold spherical nanoparticles, **(I)** MC3$^{\mu F}$ LNPs, **(J)** C12-200$^{\mu F}$ LNPs, **(K)** SM-102$^{\mu F}$ LNPs, and **(L)** ALC-0315$^{\mu F}$ LNPs. P(r) analyses and DENSS reconstructions for bulk mixed LNPs could not be generated due to their larger size ($q_{min} > \frac{2\pi}{D_{max}}$). Source data are provided as a Source Data file.

Evaluation and correlation in biological models

Current efforts to formulate next-generation LNPs rely on high-throughput screening of hundreds or thousands of unique LNPs to identify promising candidates for the desired biological application[46,47]. Due to a lack of structure-activity relationships between the lipid components and mRNA translation, lipid and LNP design are often randomly explored leading to a large percentage of the tested library to perform poorly. Attempts to correlate biological performance with LNP physicochemical characteristics and structure have yielded unsatisfactory associations because of the utilization of low-resolution analytical techniques such as DLS. Thus, we set out to determine whether our modern solution-based biophysical techniques could reveal stronger correlations between LNP characteristics and efficacy. As it has been demonstrated that the essential physicochemical parameters for effective mRNA translation depend on the biological environment, we evaluated our lipid library in three different models: primary human T cells, intravenous (IV) administration, and intramuscular (IM) administration. CD4+ and CD8+ T cells (1:1) were obtained from healthy human donors and activated for 24 h using CD3/CD28 human Dynabeads^{TM}. Afterwards, the four microfluidically mixed and four bulk mixed LNPs encapsulated FLuc mRNA were incubated with the T cells for 24 h. Afterwards, luminescent signal and viability were analyzed (Figure 7A–B). While the MC3$^{\mu F}$, SM-102$^{\mu F}$, and ALC-0315$^{\mu F}$ LNPs had 2–3 fold higher luminescent signal than their bulk mixed counterparts, the C12-200^{Bulk} LNPs outperformed the C12-200$^{\mu F}$ LNPs by almost 3-fold and was the highest performing LNP out of the library. Additionally, except for the C12-200 LNPs which had similar cellular viabilities of ~80%, the bulk mixed LNPs had 10–20% higher viability than the microfluidically mixed versions.

Upon injecting the FLuc LNPs intravenously into C57BL/6 mice and analyzing liver luminescence after 6 h, the transfection trends mirrored the T cell results (Figure 7C–D). The MC3$^{\mu F}$, SM-102$^{\mu F}$, and ALC-0315$^{\mu F}$ LNPs induced 2–3 fold higher liver luminescence signal than the bulk mixed LNPs, whereas the C12-200^{Bulk} LNP outperformed C12-200$^{\mu F}$ LNP by 3-fold. In contrast, intramuscular administration resulted in much closer luminescence in the injection site between the microfluidic and bulk mixed LNPs, with no statistically significant difference (Figure 7E–F). Still, the non-C12-200 microfluidically mixed LNPs had slightly higher luminescence than the bulk mixed counterparts, whereas C12-200^{Bulk} LNP was marginally lower than the C12-200$^{\mu F}$ LNP.

The physicochemical information of the LNP library obtained from both the traditional techniques and emerging biophysical analyses were correlated with the corresponding luminescence readouts in human primary T cells, IV administration, and IM administration. Utilizing Spearman correlations, with $r > 0.6$ or $r < -0.6$ as a threshold for medium-to-strong correlation, several physicochemical factors emerged as having strong correlation with biological outcome – although this greatly depended on the biological environment (Figure 7G–J; Supplementary Table 5). For example, T cell and IV administration had strong positive correlation with the intensity of the average SEC-SAXS peak (I_p^{Avg}), with both the SVD0 (I_p^{SVD0}) and SVD1 (I_p^{SVD1}) peaks also correlating with the T cell data but not the IV data. When comparing LNP groups based on formulation method, the intensity also is predictive of LNP performance, where the formulation method with the stronger peak always induced greater mRNA translation in T cells and IV delivery. This may explain the counterintuitive C12-200 results, as the bulk mixed formulation elicits a strong peak compared to the microfluidic formulation (Figure 7K). In contrast, I_p^{SVD0} and I_p^{SVD1} produced a strong negative correlation with the IM data, revealing an inverse relationship. Moreover, the T cell and IV biological results had a strong positive correlation with the area of the SAXS peak, particularly for the average peak ($Area^{Avg}$), with T cells also showing a significant relationship with the SVD0 peak area ($Area^{SVD0}$) and SVD1 peak area ($Area^{SVD1}$). Between these biological models, the T cell, but not IV results, also correlated with the position of the SAXS peak maximum at 0.1–0.2 q for SVD1 (q^{SVD1}), with lower q indicating more efficacious delivery.

For light scattering and other analytical techniques, the correlations also varied depending on the biological model. Encapsulation efficiency and nucleic acid number were determinant factors for T cells, but not the *in vivo* models. Additionally, pK_a has a strong correlation for IM delivery but not IV nor T cell delivery. In contrast to the canonical view of nanoparticles, LNP hydrodynamic radius (R_h) or geometric radius ($R_{geometric}$) was a poor predictor of performance for all three biological models. Instead, polydispersity from MALS was a more accurate measure, with lower M_w/M_n correlating with stronger luminescence than size. Counterintuitively, for IV delivery, PDI has a strong positive correlation, indicating inconsistency between the MALS and DLS measurements. These results reveal the significance of multiple orthogonal analytical techniques in providing correlations to LNP biological results, especially those that provide higher resolution measurements, such as FFF-MALS and SEC-SAXS. These latter techniques also have the benefit of providing information on multiple parameters from single runs in an automated fashion, significantly enhancing the throughput of the analyses. Lastly, the stark differences in correlations within the three models highlight the need to tailor particular properties depending on the biological environment, and that a one-size-fits-all approach to optimizing LNPs will not yield success in all applications.

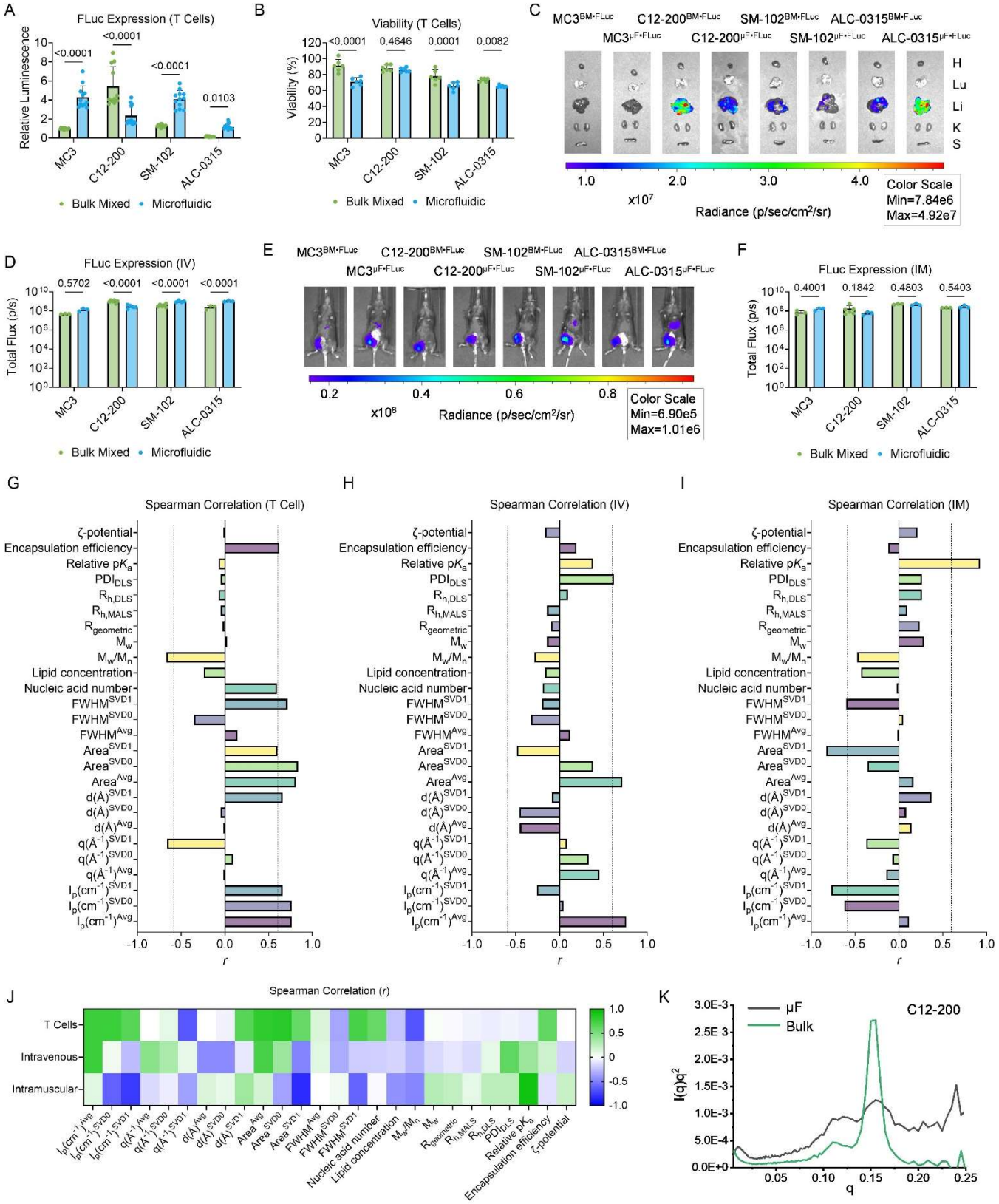

Figure 7. Lipid nanoparticle transfection in biological models and correlation with physicochemical parameters. A–B, MC3, C12-200, SM-102, and ALC-0315 LNPs, either bulked or microfluidically mixed with firefly luciferase mRNA, were incubated in 1:1 CD4+:CD8+ human primary T cells obtained from healthy donors at a dose of 300 ng per 50,000 cells. After 24 h, **(A)** luminescence and **(B)** viability were quantified. Relative luminescence and viability are reported as mean ± SD of *n* = 9. **C–D,** The eight LNPs were administered intravenously into C57BL/6J mice at a dose of 0.1 mg of mRNA per kg (mpk). After 6 h, the mice were dissected and organ luminescence was **(C)** imaged and **(D)** quantified using an in vivo imaging system (IVIS). Heart (H), lungs (Lu), liver (Li), kidneys (K), and spleen (S), were dissected and analyzed. Total flux is reported as mean ± SD of *n* = 6 for the C12-200 groups and *n* = 3 for all other groups. **E–F,** The eight LNPs were also administered intramuscularly into C57BL/6J mice at a dose of 0.05 mpk. After 6 h, the mice were

dissected and organ luminescence was **(E)** imaged and **(F)** quantified using IVIS. Total flux is reported as mean ± SD of n = 6 for the C12-200 bulk mixed and n = 3 for all other groups. **G–J,** Spearman correlations for the **(G)** T cell, **(H)** intravenous, and **(I)** intramuscular luminescence values utilizing the physicochemical parameters from the traditional, FFF-MALS, and SEC-SAXS methods, with **(J)** a heat map representing the entire data set. For the Spearman correlation graphs, dotted lines represent $r = -0.6$ and 0.6. **K**, Example Kratky plot of C12-200$^{\mu F}$ and C12-200^{bulk} LNPs obtained via SEC-SAXS. **A–B,D,F,** Two-way ANOVA with *post hoc* Holm–Šídák correction for multiple comparisons were used to compare bulk mixed against microfluidically mixed luminescent values for each LNP group. Source data are provided as a Source Data file.

Discussion

There are many limitations to the application of DLS to the characterization of nanoparticles at the length scales observed in this study. From Rayleigh scattering theory, the intensity of scattered light varies with sixth power of the particle radius. Hence, resolving smallest species from the largest, even in small amounts, can additionally confound reliable analyses of heterogenous mixtures. Very large particle sizes can also lead to multiple scattering effects, where scattered light is additionally scattered by other large particles, further complicating analysis. DLS analysis typically assumes sphericity, where shape anisotropy is not well resolved, and conventional 90° DLS instruments are not ideal for large particles that scatter light anisotropically at low angles. These considerations are paramount to the application of DLS to the extensive characterization of LNP formulations by regulatory bodies like the Food and Drug Administration (FDA) for applications and licenses that require reliable determinations of particle sizes and distributions and encapsulation efficiency, alongside evaluation of stability in storage conditions, especially since methods like DLS and RiboGreen are prescribed by regulatory agencies. Our findings suggest that the more rigorous methods applied, such as FFF-MALS and SEC-SAXS, provide superior quantitative measures of these attributes needed for these filings and human trials.

Our results demonstrate that for four formulations encapsulated with the same mRNA cargo, different spatial properties are observed, indicating that lipid composition and formulation are strong determinants of particle shape, rather than the payload. In nature, anisotropic shapes correlate with increased surface-to-volume (S/V) ratios, which is a parameter that affects macromolecular interactions. This parameter has been related to nanoparticle performance as well[48,49]. How shape affects the different aspects of LNP activity, such as uptake, targeting, payload release, potency, has only recently been appreciated[32,50,51]. The application of SAXS as described in our work here provides an avenue to quantitatively interrogate this parameter in formulations. The S/V could be a key parameter with regards to the interactions of mRNA-loaded LNPs with their target cells. A higher S/V ratio increases the surface area available for interactions with the cell membrane, thereby enhancing the likelihood of productive encounters and promoting efficient endocytosis. Smaller LNPs with high S/V ratios would be expected to diffuse more rapidly through the extracellular matrix, reducing resistance to movement and enabling them to reach the target cells more efficiently.

Along with overall shape, the internal shape of the lipid-RNA interaction is a strong determinant factor for RNA translation, as demonstrated by our Spearman correlation results. For successful transfection, the RNA cargo must break through the endosomal-lysosomal pathway, which is achieved partially due to the positively charged ionizable lipids intercalating with the endosomal phospholipid bilayers. Tighter interactions between the RNA and lipid may point to lipids shuttling the RNA as they penetrate these bilayers, although further structural analysis would be needed to confirm this. The strong correlations of I_q with T cell transfection point to the importance of structure, as *in vitro* conditions are the most simplistic as LNPs do not need to transverse physiological highways to reach their target. Instead, almost all cells will internalize the LNPs, whereas only a subset of RNAs will be translated into functional proteins; thus, the LNPs that can facilitate endosomal escape due to their internal mesophase will be at an advantage. More broadly, our correlation analyses point to a significant role of the biological environment in determining which physicochemical parameters are most essential for efficacious mRNA delivery. LNPs that immediately enter the bloodstream are coated in a complex protein corona that directly impacts both their uptake pathway and endosomal escape, while intramuscular routes proceed largely via the lymphatic system and thus subject to immune cell uptake.

When comparing the microfluidic and bulk mixing techniques, clear differences emerge, despite utilizing the same excipients and molar ratios in each formulation. The 1X PDMS microfluidic devices increase the relative

encapsulation efficiency, and despite being smaller in size, have similar or greater nucleic acid copy numbers, except for SM-102^{Bulk}, which has almost a tenfold higher number than SM-102$^{\mu F}$. All FDA-approved LNPs have enhanced mRNA transfection in the three biological models tested when microfluidically prepared, whereas C12-200^{Bulk} achieving superior delivery compared to C12-200$^{\mu F}$. This suggests that the structure of the lipid components may be an important parameter in choosing the formulation method. Still, when fabricating microfluidic devices, there are several degrees of freedom that can be optimized depending on the LNP recipe. It is likely feasible to optimize device composition, geometry, and flow to achieve specific LNP physicochemical properties, shape, and internal ordering; however, the structure of the lipid will need to be included as a tertiary factor. As microfluidic formulation offers a path towards global scale up of LNP therapeutics, as has been demonstrated with our devices, effort should be placed on how physicochemical characteristics are altered on both small and large scales[52].

In summary, we present a set of solution-based biophysical techniques that can analyze LNP polydispersity, composition, size, and shape with higher resolution. When paired with biological data, these analytical tools offer the ability to create rulesets that may help guide future LNP rationale design by establishing structure-activity relationships based on the physicochemical properties. Future studies will aim to perform the same high-caliber biophysical analysis on isolated LNP subspecies to gauge how certain species within a single batch of an LNP formulation contribute to the overall toxicity and efficacy.

Methods

All animal use was in accordance with the guidelines and approval from the University of Pennsylvania's Institutional Animal Care and Use Committee (IACUC; protocol #806540).

Materials

Lipid excipients were obtained from Avanti Polar Lipids (Alabaster, AL, USA). Firefly luciferase mRNA was purchased from TriLink Biotechnologies (San Diego, CA, USA) and contained 5-methoxyuridine substitutions. Dialysis cassettes and pH 7.4 10X PBS were obtained from Thermo Fisher Scientific (Waltham, MA, USA). Citrate buffer was purchased from Teknova (Hollister, CA, USA). Syringe filters were obtained from Genesee Scientific (El Cajon, CA, USA).

Lipid nanoparticle preparation

Lipid excipients were dissolved in ethanol, utilizing the following molar ratios:
MC3 LNPs: D-Lin-MC3-DMA (50 mol%), DSPC (10 mol%), cholesterol (38.5 mol%), and DMG-PEG2000 (1.5 mol%).
C12-200 LNPs: C12-200 (35 mol%), DOPE (16 mol%), cholesterol (46.5 mol%), and C14-PEG2000 (2.5 mol%).
SM-102 LNPs: SM-102 (50 mol%), DSPC (10 mol%), cholesterol (38.5 mol%), and DMG-PEG2000 (1.5 mol%).
ALC-0315 LNPs: ALC-0315 (46.3 mol%), DSPC (9.4 mol%), cholesterol (42.7 mol%), and ALC-0159 (1.6%).

Firefly luciferase mRNA was dissolved in 10 mL citrate buffer at pH 3. Each LNP was formulated utilizing an IL-to-mRNA weight ratio 10:1 with a volume ratio of aqueous phase to organic phase of 3:1. For the microfluidically mixed LNPs, each phase was loaded into separate glass syringes (Hamilton Company, Reno, NV, USA) and attached to a Pump 33 DDS syringe pump (Harvard Apparatus, MA, USA). The liquid phases were pushed through a staggered herringbone micromixer microfluidic device, fabricated via polydimethylsiloxane via soft lithography[13]. A two-step exposure process was used to create the SU-8 master with positive channel features on a silicon wafer, where each mixing channel is 4 cm in length. The glass syringes were injected at a flow rate of 0.6 mL/min and 1.8 mL/min for the organic phase and aqueous phase, respectively. The empty LNPs were prepared via the microfluidic device as described above, but without mRNA in the citrate phase. For bulk mixed LNPs, the ethanol and aqueous phases were transferred to a 1.5 mL microcentrifuge tube using a repeater pipette and was mixed for 50 cycles at 0.1 mL. All LNPs were dialyzed against pH 7.4 1X PBS in 20 kDa MWCO cassettes for a minimum of 2 h at room temperature. Afterwards, the microfluidically mixed LNPs were passed through a 220 nm filter and the bulk mixed were passed through a 450 nm filter, and then were stored at 4 °C.

Measuring lipid nanoparticle encapsulation and pK_A

Relative encapsulation efficiency and encapsulated mRNA concentration were determined via a Quant-iT RiboGreen Assay (Thermo Fisher Scientific). Briefly, LNPs were diluted 100-fold in either 1X tris-EDTA (TE) buffer (Thermo Fisher Scientific) or 1X TE buffers supplemented with 1% (v/v) Triton X-100 (Alfa Aesar, Haverhill, MA, USA). The LNPs equilibrated in the buffers for 5 min before being transferred to a black 96-well plate (Corning). A standard curve was prepared according to the manufacturer's instructions. The RiboGreen reagent was mixed 1:1 (v/v) with the standard curve and LNP solution and equilibrated for 5 min. Afterwards, fluorescence intensity was read on an Infinite 200 Pro plate reader (Tecan, Morrisville, NC) at an excitation wavelength of 490 nm and an emission wavelength of 530 nm. RNA content was quantified via the standard curve estimated from a univariate least squares linear regression (LSLR). Encapsulation efficiency was calculated as $EE = \frac{B-A}{A} \cdot 100\%$, where A is the measured RNA content in TE buffer and B is the measured RNA content in post-lysis. The encapsulated mRNA concentration was calculated by $[conc] = B - A$. Encapsulation efficiencies and mRNA concentrations are reported as mean ± standard deviation using n = 4 technical replicates.

The relative pK_a of the LNPs was determined by a 6-(p-toluidinyl)napthalene-2-sulfonic (TNS) assay. LNPs were diluted 3-fold in pH 7.4 1X PBS. Buffers containing 150 mM sodium chloride, 20 mM sodium phosphate, 20 mM ammonium acetate, and 25 mM ammonium citrate were adjusted to pH 2 to pH 11 in increments of 0.5 pH units. The TNS solution was prepared by dissolving TNS to a concentration of 160 µM in DI water. In a black 96-well plate (Corning) was added 125 µL of each pH-adjusted solution, 2.5 µL of each LNP formulation, and 5 µL of the TNS solution. The plate was then shaken in the dark at 200 rpm for 5 min. Afterwards, fluorescence was measured on an Infinite 200 Pro plate reader (Tecan) at an excitation wavelength of 322 nm and an emission wavelength of 431 nm. Using univariate LSLR, the pK_a was determined as the pH corresponding to the half-maximum fluorescence intensity, which corresponds to 50% protonation.

Dynamic light scattering

Hydrodynamic radius, polydispersity (PDI), and particle concentration were obtained using a DynaPro Plate Reader III (Wyatt Technology, LLC) using a cumulants model. The LNPs were diluted 50-fold in pH 7.4 1X PBS, where 30 µL were loaded onto a 384-well Aurora plate (Wyatt Technology, LLC.). The plate was centrifuged for 5 min at 300 g and then loaded onto the plate reader. Size is reported as intensity-weighted averages with n = 3 measurements, and data is expressed as mean ± standard deviation, where the standard deviation is calculated by $STD = \sqrt{PDI} \cdot radius$. LNP PDI and concentration are reported as mean ± standard deviation of n = 3 measurements.

Zeta potential

Batch DLS, SLS and ELS measurements were conducted on a DynaPro ZetaStar™ instrument (Wyatt Technology, LLC.). The instrument is equipped with a 785 nm laser and individually optimized detectors for dynamic, static, and electrophoretic light scattering measurements. The neat LNPs were diluted 100-fold in 0.02 µm filtered 20 mM Tris, pH 7.4, loading 65 µL sample into the ZetaStar dip cell. Data acquisition and analysis were performed with DYNAMICS™ software 8.3.1. (Wyatt Technology, LLC.). Adaptive collection mode was used to optimize the applied current and measurement time. The resulting measurement time was on average 60 seconds. The reported results are averages and standard deviations from n = 10 measurements.

Cryogenic transmission electron microscopy

Morphology and size were analyzed by cryo-TEM by adding 3 µL of the LNPs at an mRNA concentration of 50 ng/µL to a Quantifoil™ (Jena, Germany) holey carbon grid which had been glow discharged. Grids were blotted and frozen in liquid ethane using a Vitrobot™ Mark IV (Thermo Fisher Scientific). Imaging was performed at the Beckman Center for cryo-EM on a Titan Krios™ equipped with a K3 Bioquantum (Thermo Fisher Scientific).

Sedimentation velocity analytical ultracentrifugation

Sedimentation velocity analytical ultracentrifugation experiments were performed at 20°C with an Optima™ analytical ultracentrifuge (Beckman-Coulter, Brea, CA) and a TiAn50 rotor with two-channel charcoal-filled Epon centerpieces and sapphire windows, using both absorbance and interference optics. Data were collected in 1x PBS with detection at 260 & 280 nm, as well as interference optics. Complete sedimentation velocity profiles were recorded every 30 seconds at 20,000 rpm and 20°C. Data were fit using a least-squares g*(s) model as implemented in the program SEDFIT[53].

Asymmetric-flow field-flow fractionation measurements

Samples were injected undiluted in triplicates on an Eclipse™ field flow fractionation (FFF) instrument using a 350 µm fixed-height short channel with dilution control module and a 10 kDa regenerated cellulose membrane (Wyatt Technology, LLC.), connected to a 1260 Infinity II HPLC system with a G1310B isocratic pump and a G1329B autosampler (Agilent Technologies, Inc.). A DAWN™ MALS instrument with an integrated WyattQELS™ DLS detector (Wyatt Technology, LLC.), an Optilab™ differential refractometer (Wyatt Technology, LLC.), and a G1365C UV detector (Agilent Technologies, Inc.) set to 260 nm wavelength were used for online detection. 1X PBS at pH 7.4 was used as the mobile phase. Sample injection volume: 55–150 µL. The FFF system was controlled by VISION 3.2.0 software (Wyatt Technology, LLC.). FFF method parameters: 2.5 mL/min channel flow and 0.5 mL/min detector flow (corresponding to a 5-fold concentration enhancement from the dilution control module), 0.1 mL/min inject flow. Focusing was at 1.0 mL/ min with a 25% focus position for 14 min. Cross flow was ramped from 0 to 1.0 mL/min in the first minute of the method, and then kept constant at 1.0 mL/min throughout focusing and the initial 5 min of the elution step, followed by an exponential gradient of 1.0–0.04 mL/min over 30 min after which the crossflow was kept constant at 0.04 mL/min for 15 min before being turned off. Prior to LNP sample injections, the membrane was conditioned by injecting 100 µL of a 2 mg/mL bovine serum albumin (BSA) standard (Wyatt Technology, LLC.). The system performance was checked by injecting and analyzing a triplicate of 25 µL of the same BSA standard using the BSA short channel FFF method built into the VISION 3.2.0 software. The online MALS detectors were calibrated at 90° scattering angle and the remaining detector angles normalized to the response at 90° using the BSA monomer peak data. Data acquisition and analysis were performed using the LNP Analysis Module in the ASTRA™ 8.2.2 software (Wyatt Technology, LLC.). Blank injections of mobile phase were used for RI signal baseline subtraction. To obtain accurate concentration data from the online 260 nm UV absorbance signal, empty LNP samples were also prepared microfluidically with lipid compositions and concentrations matching the LNP-mRNA samples. The empty LNP samples were measured with the same FFF method as the LNP-mRNA samples, and the results from the empty samples were used to generate experimentally derived UV scattering correction profiles with the ASTRA LNP Analysis Module. The scattering correction profiles were then applied non-destructively to the data collected for the corresponding LNP-mRNA samples.

Synchrotron size-exclusion chromatography in line with small angle X-ray scattering

Size-exclusion chromatography (SEC)-SAXS data were collected at beamline 16-ID (LiX) of the National Synchrotron Light Source II (Upton, NY)[54–56]. SAXS/WAXS data were simultaneously collected at a wavelength of 0.89 Å, yielded accessible scattering angle where $0.005 < q < 3.0$ Å^{-1}, where q is the momentum transfer, defined as $q = 4\pi \frac{\sin(\theta)}{\lambda}$, where λ is the X-ray wavelength and 2θ is the scattering angle; data to $q<0.5$ Å^{-1} were used in subsequent analyses. 100 µL of LNP at a particle concentration of ~10^{11} particles were injected and eluted isocratically at 0.35 ml/min from a prepared 3 mL Sepharose 4B sizing column equilibrated in 1X PBS (Invitrogen), at room temperature. Eluent from the column flowed into a 1 mm capillary for subsequent X-ray exposures at 2-s intervals. Plots of intensity from the forward scatter closely correlated to in-line UV and refractive index (RI) measurements.

Small angle X-ray scattering analysis

SVD-EFA analysis of the SEC-SAXS data sets were performed, as implemented in the program RAW[57]. Buffer subtracted profiles were analyzed by singular value decomposition (SVD) and the ranges of overlapping peak data determined using evolving factor analysis (EFA)[58] as implemented in REGALS[40]. The determined peak windows were used to identify the basis vectors for each component and the corresponding SAXS profiles were calculated. When manually fitting the pair distribution function P(r), the maximum diameter of the particle (D_{max}) was incrementally adjusted in GNOM[59] as implemented in RAW[60] to maximize the Total Estimate and χ^2 figures,

to minimize the discrepancy between the fit and the experimental data to a q_{max} of 0.1 $Å^{-1}$, and to optimize the visual qualities of the distribution profile.

Deconvolution of the primary Braggs peaks in SAXS were using multiple Lorentz fits[8] with the built-in function:

$$y = y_0 + \frac{2 \times area}{\pi} \times \frac{width}{4(x - x_c)^2 + width^2}$$

where y_0 is an offset and was set to the X-ray baseline. x_c is a center of function and corresponds to the center of the SAXS peak.

Porod values were calculated using ScÅtter.

DENSS[22,42] was used to calculate the *ab initio* electron density map directly from the GNOM output. Twenty reconstructions of electron density were performed in the slow mode with default parameters and subsequently averaged and refined. Reconstructions were visualized using PyMOL 2.5.2 Molecular Graphics System (Schrodinger, LLC, New Your, NY) with five contour levels of density rendered with these respective colors: 15σ (red), 10σ (green), 5σ (cyan), 2.5σ (blue), and -0.7σ (blue). The sigma (σ) level denotes the standard deviation above the average electron density value of the generated model.

T cell studies

Human primary T cells were obtained from donors at the Human Immunology Core at the University of Pennsylvania. T cells were activated using Human T-Activator CD3/CD28 Dynabeads™ (Thermo Fisher Scientific) at a bead-to-cell ratio of 1:1 for 24 h. Then, the T cells were plated onto white 96-well plates (Corning, Corning, New York, USA) at a density of 60,000 cells per well. Immediately afterwards, the cells were treated with LNPs containing FLuc mRNA at a dose of 300 ng per well. Following 24 h of incubation, the plates were centrifuged at 400 g for 5 min to pellet the cells. Then, luminescence and viability were ascertained via Promega (Madison, WI, USA) Luciferase Assay System and Cell-titer Glo(R) Luminescent Cell Viability Assay, respectively, according to the manufacturer's instructions. Data were normalized to $MC3^{Bulk•FLuc}$ and was reported as mean ± SD of four technical replicates from n = 3 donors.

Murine biodistribution

C57BL/6J female mice of 6-8 weeks old with an average weight of 20 g were purchased from Jackson Laboratory (Bar Harbor, ME). Animals were housed in a barrier facility with air humidity 40%–70%, ambient temperature (22 ± 2 °C), and 12 h dark/12 h light cycle.

For intravenous studies, mice were injected with bulk and microfluidically mixed LNPs encapsulating FLuc mRNA via the lateral tail vein at a dose of 0.1 mg of mRNA per kg of body mass (mg/kg). For intramuscular studies, mice were injected with the LNPs in the left quadricep at a dose of 0.05 mg/kg. After 6 h, the mice were administered an intraperitoneal injection of D-luciferin (0.2 mL, 15 mg/mL; Biotium, Fremont, CA). Then, after 5 min, full body luminescence images were obtained using an In Vivo Imaging System (IVIS; PerkinElmer, Waltham, MA) for the intramuscular group only. For the intravenous group, the mice were euthanized, and the heart, lungs, liver, kidneys, and spleen were removed and imaged for luminescence using IVIS. Total flux was quantified by the Living Image™ Software (PerkinElmer) by placing rectangular region of interests (ROI) around the full body or organ images, keeping the same ROI sizes among each body or organ. Total flux was reported as mean ± SD of *n* = 3 or 6 biological replicates.

Statistics & reproducibility

All statistical analysis was performed in GraphPad™ Prism Version 10.4.0 (GraphPad Software, Inc, La Jolla, USA). All tests of significance were performed at a significance level of α = 0.05. For experiments that measured two variables with more than two treatment groups, a two-way ANOVA with post hoc Holm-Šídák correction for

multiple comparisons were used to compare responses across treatment groups. All data are presented as mean ± standard deviation unless otherwise reported. No statistical method was used to predetermine sample size. No data were excluded from the analyses. The experiments were not randomized. The investigators were not blinded to allocation during experiments and outcome assessment.

Data availability

All relevant data supporting the findings of this study are available within the paper and Supplementary Information. Source data are provided with this paper. Raw AUC data is made available at the following repository link: [http:/zenodo.org]. Small-angle scattering data generated as part of this work have been deposited at the SASDB under accession codes: [codes].

Code availability

No original code was generated for this study.

References

1. Pardi, N., Hogan, M. J., Porter, F. W. & Weissman, D. mRNA vaccines-a new era in vaccinology. *Nature Reviews Drug Discovery* **17**, 261–279 (2018).
2. Hajj, K. A. *et al.* A Potent Branched-Tail Lipid Nanoparticle Enables Multiplexed mRNA Delivery and Gene Editing in Vivo. *Nano Letters* **20**, 5167–5175 (2020).
3. Finn, J. D. *et al.* A Single Administration of CRISPR/Cas9 Lipid Nanoparticles Achieves Robust and Persistent In Vivo Genome Editing. *Cell Reports* **22**, 2455–2468 (2018).
4. Walsh, G. & Walsh, E. Biopharmaceutical benchmarks 2022. *Nature Biotechnology* **40**, 1722–1760 (2022).
5. Hou, X., Zaks, T., Langer, R. & Dong, Y. Lipid nanoparticles for mRNA delivery. *Nature Reviews Materials* **6**, 1078–1094 (2021).
6. Shepherd, S. J., Issadore, D. & Mitchell, M. J. Microfluidic formulation of nanoparticles for biomedical applications. *Biomaterials* **274**, 120826 (2021).
7. Evers, M. J. W. *et al.* State-of-the-Art Design and Rapid-Mixing Production Techniques of Lipid Nanoparticles for Nucleic Acid Delivery. *Small Methods* **2**, 1700375 (2018).
8. Hammel, M. *et al.* Correlating the Structure and Gene Silencing Activity of Oligonucleotide-Loaded Lipid Nanoparticles Using Small-Angle X-ray Scattering. *ACS Nano* (2023) doi:10.1021/acsnano.3c01186.
9. Brader, M. L. *et al.* Encapsulation state of messenger RNA inside lipid nanoparticles. *Biophysical Journal* **120**, 2766–2770 (2021).
10. Kulkarni, J. A. *et al.* On the Formation and Morphology of Lipid Nanoparticles Containing Ionizable Cationic Lipids and siRNA. *ACS Nano* **12**, 4787–4795 (2018).
11. Chen, D. *et al.* Rapid discovery of potent siRNA-containing lipid nanoparticles enabled by controlled microfluidic formulation. *Journal of the American Chemical Society* **134**, 6948–6951 (2012).
12. Leung, A. K. K. *et al.* Lipid nanoparticles containing siRNA synthesized by microfluidic mixing exhibit an electron-dense nanostructured core. *Journal of Physical Chemistry C* **116**, 18440–18450 (2012).
13. Shepherd, S. J. *et al.* Scalable mRNA and siRNA Lipid Nanoparticle Production Using a Parallelized Microfluidic Device. *Nano Letters* (2021) doi:10.1021/acs.nanolett.1c01353.
14. Hallan, S. S., Sguizzato, M., Esposito, E. & Cortesi, R. Challenges in the physical characterization of lipid nanoparticles. *Pharmaceutics* **13**, 1–31 (2021).
15. Henrickson, A. *et al.* Density Matching Multi-wavelength Analytical Ultracentrifugation to Measure Drug Loading of Lipid Nanoparticle Formulations. *ACS Nano* **15**, 5068–5076 (2021).

16. Sych, T. *et al.* High-throughput measurement of the content and properties of nano-sized bioparticles with single-particle profiler. *Nature Biotechnology* (2023) doi:10.1038/s41587-023-01825-5.
17. Li, S. *et al.* Payload distribution and capacity of mRNA lipid nanoparticles. *Nature communications* **13**, 5561 (2022).
18. Li, S. *et al.* Single-Particle Spectroscopic Chromatography Reveals Heterogeneous RNA Loading and Size Correlations in Lipid Nanoparticles. *ACS Nano* **18**, 15729–15743 (2024).
19. Bizmark, N. *et al.* Ribogreen Fluorescent Assay Kinetics to Measure Ribonucleic Acid Loading into Lipid Nanoparticle Carriers. *Advanced Materials Interfaces* **11**, 2301083 (2024).
20. Filipe, V., Hawe, A. & Jiskoot, W. Critical Evaluation of Nanoparticle Tracking Analysis (NTA) by NanoSight for the Measurement of Nanoparticles and Protein Aggregates. *Pharm Res* **27**, 796–810 (2010).
21. Paloncýová, M. *et al.* Atomistic Insights into Organization of RNA-Loaded Lipid Nanoparticles. *J. Phys. Chem. B* (2023) doi:10.1021/acs.jpcb.2c07671.
22. Dao, H. M. *et al.* Characterization of mRNA Lipid Nanoparticles by Electron Density Mapping Reconstruction: X-ray Scattering with Density from Solution Scattering (DENSS) Algorithm. *Pharm Res* **41**, 501–512 (2024).
23. Vezočnik, V. *et al.* Size fractionation and size characterization of nanoemulsions of lipid droplets and large unilamellar lipid vesicles by asymmetric-flow field-flow fractionation/multi-angle light scattering and dynamic light scattering. *Journal of Chromatography A* **1418**, 185–191 (2015).
24. Guerrini, G., Mehn, D., Scaccabarozzi, D., Gioria, S. & Calzolai, L. Analytical Ultracentrifugation to Assess the Quality of LNP-mRNA Therapeutics. *International Journal of Molecular Sciences* **25**, 5718 (2024).
25. Thaller, A. *et al.* SV-AUC as a stability-indicating method for the characterization of mRNA-LNPs. *European Journal of Pharmaceutics and Biopharmaceutics* **182**, 152–156 (2023).
26. Parot, J. *et al.* Quality assessment of LNP-RNA therapeutics with orthogonal analytical techniques. *Journal of Controlled Release* **367**, 385–401 (2024).
27. Schuck, P. & Rossmanith, P. Determination of the sedimentation coefficient distribution by least-squares boundary modeling. *Biopolymers* **54**, 328–341 (2000).
28. Zhao, H., Sousa, A. A. & Schuck, P. Flotation Coefficient Distributions of Lipid Nanoparticles by Sedimentation Velocity Analytical Ultracentrifugation. *ACS Nano* **18**, 18663–18672 (2024).
29. Zhao, H., Brautigam, C. A., Ghirlando, R. & Schuck, P. Overview of Current Methods in Sedimentation Velocity and Sedimentation Equilibrium Analytical Ultracentrifugation. *Current Protocols in Protein Science* **71**, 20.12.1-20.12.49 (2013).
30. Einstein, A. Über die von der molekularkinetischen Theorie der Wärme geforderte Bewegung von in ruhenden Flüssigkeiten suspendierten Teilchen. *Annalen der Physik* **322**, 549–560 (1905).
31. Svedberg, T. & Fåhraeus, R. A NEW METHOD FOR THE DETERMINATION OF THE MOLECULAR WEIGHT OF THE PROTEINS. *J. Am. Chem. Soc.* **48**, 430–438 (1926).
32. Simonsen, J. B. A perspective on bleb and empty LNP structures. *Journal of Controlled Release* **373**, 952–961 (2024).
33. Jia, X. *et al.* Enabling online determination of the size-dependent RNA content of lipid nanoparticle-based RNA formulations. *Journal of Chromatography B* **1186**, 123015 (2021).
34. Some, D., Amartely, H., Tsadok, A. & Lebendiker, M. Characterization of Proteins by Size-Exclusion Chromatography Coupled to Multi-Angle Light Scattering (SEC-MALS). *JoVE (Journal of Visualized Experiments)* e59615 (2019) doi:10.3791/59615.
35. Gao, Z. *et al.* Development of an advanced separation and characterization platform for mRNA and lipid nanoparticles using multi-detector asymmetrical flow field-flow fractionation. *Anal Bioanal Chem* (2024) doi:10.1007/s00216-024-05455-x.
36. Pabst, G., Rappolt, M., Amenitsch, H. & Laggner, P. Structural information from multilamellar liposomes at full hydration: Full q-range fitting with high quality x-ray data. *Phys. Rev. E* **62**, 4000–4009 (2000).
37. Graewert, M. A. *et al.* Quantitative size-resolved characterization of mRNA nanoparticles by in-line coupling of asymmetrical-flow field-flow fractionation with small angle X-ray scattering. *Sci Rep* **13**, 15764 (2023).

38. Kulkarni, C. V., Yaghmur, A., Steinhart, M., Kriechbaum, M. & Rappolt, M. Effects of High Pressure on Internally Self-Assembled Lipid Nanoparticles: A Synchrotron Small-Angle X-ray Scattering (SAXS) Study. *Langmuir* **32**, 11907–11917 (2016).
39. Uebbing, L. *et al.* Investigation of pH-Responsiveness inside Lipid Nanoparticles for Parenteral mRNA Application Using Small-Angle X-ray Scattering. *Langmuir* **36**, 13331–13341 (2020).
40. Meisburger, S. P., Xu, D. & Ando, N. REGALS: a general method to deconvolve X-ray scattering data from evolving mixtures. *IUCrJ* **8**, 225–237 (2021).
41. Hura, G. L. *et al.* Comprehensive macromolecular conformations mapped by quantitative SAXS analyses. *Nat Methods* **10**, 453–454 (2013).
42. Grant, T. D. Ab initio electron density determination directly from solution scattering data. *Nat Methods* **15**, 191–193 (2018).
43. Schmidt, P. W. Small-angle scattering studies of disordered, porous and fractal systems. *J Appl Cryst* **24**, 414–435 (1991).
44. Xia, X. *et al.* Quantitative determining interface information of nano composite by synchrotron radiation small-angle X-ray scattering. *Composites Part B: Engineering* **120**, 92–96 (2017).
45. Johansen, D., Trewhella, J. & Goldenberg, D. P. Fractal dimension of an intrinsically disordered protein: Small-angle X-ray scattering and computational study of the bacteriophage λ N protein. *Protein Science* **20**, 1955–1970 (2011).
46. Guimaraes, P. P. G. *et al.* Ionizable lipid nanoparticles encapsulating barcoded mRNA for accelerated in vivo delivery screening. *Journal of Controlled Release* **316**, 404–417 (2019).
47. Rhym, L. H., Manan, R. S., Koller, A., Stephanie, G. & Anderson, D. G. Peptide-encoding mRNA barcodes for the high-throughput in vivo screening of libraries of lipid nanoparticles for mRNA delivery. *Nat. Biomed. Eng* 1–10 (2023) doi:10.1038/s41551-023-01030-4.
48. Abbasi, R., Shineh, G., Mobaraki, M., Doughty, S. & Tayebi, L. Structural parameters of nanoparticles affecting their toxicity for biomedical applications: a review. *J Nanopart Res* **25**, 43 (2023).
49. Öztürk, K., Kaplan, M. & Çalış, S. Effects of nanoparticle size, shape, and zeta potential on drug delivery. *International Journal of Pharmaceutics* **666**, 124799 (2024).
50. Pattipeiluhu, R. *et al.* Liquid crystalline inverted lipid phases encapsulating siRNA enhance lipid nanoparticle mediated transfection. *Nat Commun* **15**, 1303 (2024).
51. Zheng, L., Bandara, S. R., Tan, Z. & Leal, C. Lipid nanoparticle topology regulates endosomal escape and delivery of RNA to the cytoplasm. *Proceedings of the National Academy of Sciences* **120**, e2301067120 (2023).
52. Shepherd, S. J. *et al.* Throughput-scalable manufacturing of SARS-CoV-2 mRNA lipid nanoparticle vaccines. *Proceedings of the National Academy of Sciences* **120**, e2303567120 (2023).
53. Schuck, P. Size-Distribution Analysis of Macromolecules by Sedimentation Velocity Ultracentrifugation and Lamm Equation Modeling. *Biophysical Journal* **78**, 1606–1619 (2000).
54. DiFabio, J. *et al.* The life science x-ray scattering beamline at NSLS-II. *AIP Conference Proceedings* **1741**, 030049 (2016).
55. Yang, L. *et al.* Tools for supporting solution scattering during the COVID-19 pandemic. *J Synchrotron Rad* **28**, 1237–1244 (2021).
56. Yang, L. *et al.* Solution scattering at the Life Science X-ray Scattering (LiX) beamline. *J Synchrotron Rad* **27**, 804–812 (2020).
57. Hopkins, J. B., Gillilan, R. E. & Skou, S. BioXTAS RAW: improvements to a free open-source program for small-angle X-ray scattering data reduction and analysis. *Journal of Applied Crystallography* **50**, 1545 (2017).
58. Maeder, Marcel. Evolving factor analysis for the resolution of overlapping chromatographic peaks. *Anal. Chem.* **59**, 527–530 (1987).
59. Svergun, D. I. Determination of the regularization parameter in indirect-transform methods using perceptual criteria. *J Appl Cryst* **25**, 495–503 (1992).

60. Semenyuk, A. V. & Svergun, D. I. GNOM – a program package for small-angle scattering data processing. *J Appl Cryst* **24**, 537–540 (1991).

Acknowledgments

M.S.P. acknowledges support from the National Institute of Dental & Craniofacial Research (NIDCR) of the National Institutes of Health (NIH) under Award Number T90DE030854 and the Center for Innovation & Precision Dentistry (CiPD) at the University of Pennsylvania. The content is solely the responsibility of the authors and does not necessarily represent the official views of the National Institutes of Health. K.G. acknowledges support from the Johnson Research Foundation and NIH Shared Instrumentation Grant S10-OD018483. The SV-AUC and DLS experiments were performed at the Johnson Foundation Biophysical and Structural Biology Core Facility (University of Pennsylvania, Philadelphia PA). The LiX beamline is part of the Center for BioMolecular Structure (CBMS), which is primarily supported by the National Institutes of Health, National Institute of General Medical Sciences (NIGMS) through a P30 Grant (P30GM133893), and by the DOE Office of Biological and Environmental Research (KP1605010). LiX also received additional support from NIH Grant S10 OD012331. As part of NSLS-II, a national user facility at Brookhaven National Laboratory, work performed at the CBMS is supported in part by the U.S. Department of Energy, Office of Science, Office of Basic Energy Sciences Program under contract number DE-SC0012704. Additionally, the authors thank Emily Cento, Zhilin Chen, Max A. Eldabbas, and Emileigh Maddox of the Human Immunology Core and the Division of Transfusion Medicine and Therapeutic Pathology at the Perelman School of Medicine at the University of Pennsylvania for providing de-identified CD4+ and CD8+ T cells that were purified from healthy donor apheresis using StemCell RosetteSep™ kits. The HIC is supported in part by NIH P30 AI045008 and P30 CA016520. HIC RRID: SCR_022380. Cryo-EM imaging was provided by the Beckman Center for Cryo Electron Microscopy at the University of Pennsylvania Perelman School of Medicine (RRID: SCR_022375). M.J.M. acknowledges support from a US National Institutes of Health (NIH) Director's New Innovator Award (DP2 TR002776), a Burroughs Wellcome Fund Career Award at the Scientific Interface (CASI), an American Cancer Society Research Scholar Grant (RSG-22-122-01-ET), and a US National Science Foundation CAREER Award (CBET-2145491).

Author Contributions

M.S.P., S.J.S., M.K., X.Z., M.C., J.B., and K.G. conceived and designed the experiments. M.S.P., S.J.S., A.H., M.K., X.Z., J.B., H.M.Y., A.R., R.A.J., and K.M. performed the experiments. M.S.P., S.J.S., M.K., X.Z., M.C., J.B., and K.G. analyzed the data. M.S.P. and K.G. wrote the manuscript. D.I. and M.J.M. edited the manuscript. All authors discussed the results and commented on the manuscript.

Competing Interests

The authors declare that they have no conflicts of interest with the contents of this article.